Materials Today • Volume xxx, Number xx • xxxx 2024

ELSEVIER

Polydopamine-armed microalgal oxygenerator targeting the hypoxia-adenosine axis to boost cancer photothermal immunotherapy

Cheng Zhang [1], Zi-Yi Han [1], Ke-Wei Chen, Yu-Zhang Wang, Xiao Yan, Xian-Zheng Zhang

Key Laboratory of Biomedical Polymers of Ministry of Education & Department of Chemistry, Wuhan University, Wuhan 430072, PR China

Hypoxia induces the generation of immunosuppressive adenosine within the tumor microenvironment (TME) and further impedes the activation of antitumor immunity triggered by photothermal therapy (PTT). In this study, a photothermal microalgae system (PTA) based on *Chlorella sorokiniana* (*C. soro*) is developed to boost antitumor immune responses by targeting the hypoxia-adenosine axis. PTA is constructed by coating polydopamine (PDA), a promising photothermal agent with good biocompatibility, on the surface of *C. soro*. Due to the inherent photosynthetic capability of microalgae, PTA in situ generates O_2 within the tumor under irradiation at 660 nm for hypoxia alleviation, thereby downregulating the level of adenosine to reverse the immunosuppression in TME. Subsequently, this reshaped TME promotes the activation of antitumor immunity induced by PTT, which is realized by the coated PDA layer on *C. soro* under irradiation at 808 nm. In a mouse model of 4T1 tumors, PTA significantly weakens the immunosuppression in the TME, elicits robust antitumor immune responses, and suppresses tumor growth. Together, this strategy highlights the potential of leveraging living photosynthetic microalgae as an oxygenerator to boost cancer photothermal immunotherapy.

Keywords: Microalgae; Polydopamine; Adenosine; Cancer; Immunotherapy

Introduction

Insufficient oxygen supply can lead to hypoxia in various rapidly growing solid tumors, resulting in transformation of the tumor microenvironment (TME) into a highly immunosuppressive setting [1–4]. In response to hypoxia, cancer cells upregulate the expression of hypoxia-inducible factor 1α (HIF-1α), which subsequently enhances the expression of ectonucleotidases CD39 and CD73 [5]. Specifically, CD39 converts extracellular adenosine triphosphate (ATP) to adenosine monophosphate (AMP), and CD73 further dephosphorylates AMP to adenosine within the tumor [6]. Adenosine then binds to A2A adenosine receptors (A2ARs) on immune cells, shifting the TME from an immunopermissive state to an immunosuppressive state by inhibiting the function of T lymphocytes, promoting the activity of myeloid-derived suppressor cells (MDSCs), and polarizing tumor-associated macrophages (TAMs) into an immunosuppressive M2 phenotype [7–9]. The immunosuppressive TME often reduces the effectiveness of various cancer therapies that induce immunogenic cell death (ICD) and release tumor-associated antigens (TAAs), such as chemotherapy, radiotherapy, photodynamic therapy, and photothermal therapy [10–17]. Therefore, targeting the hypoxia-adenosine axis is a promising strategy to overcome TME barriers for effective anticancer immunity.

In recent years, several approaches have been developed to modulate the TME by targeting the hypoxia-adenosine axis. For example, inhibition of HIF-1α, CD39, CD73, and A2ARs using inhibitors or antibodies has successfully promoted antitumor

[1] These authors contributed equally.
E-mail address: Zhang, X.-Z. (xz-zhang@whu.edu.cn)

 https://doi.org/10.1016/j.mattod.2024.04.001

Please cite this article in press as: C. Zhang et al., Materials Today (2024), https://doi.org/10.1016/j.mattod.2024.04.001

immunity [18–24]. However, complete reversion of immunosuppression is often challenging to achieve. Instead of focusing on downstream target sites, directly oxygenating hypoxic tumors through respiratory hyperoxia (60 % O_2) represents an alternative strategy to address the root cause of hypoxia-induced immunosuppression in the TME [7]. Nevertheless, this approach requires expensive medical equipment and may cause hyperoxia-related damage to patients. In recent years, nanotechnology for biomedical applications has been rapidly developed [25–27]. Various synthetic materials have been designed to alleviate hypoxia by delivering exogenous O_2 into tumors or by in situ generation of O_2 through intratumoral H_2O_2 decomposition or photocatalytic H_2O splitting [28–34]. However, their efficacy is hindered by limited exogenous O_2 loading capacity, restricted intratumoral H_2O_2 concentration, and the degradation and clearance of photocatalysts. Therefore, there is an urgent need for a convenient, efficient, and sustainable O_2 supply strategy to alleviate hypoxia within tumors.

In nature, approximately 50 % of the Earth's atmospheric O_2 is produced through photosynthesis by microalgae [35,36]. These microorganisms, which have evolved over thousands of years, possess a sophisticated and resilient photosynthetic system that operates effectively and reliably in diverse and challenging environments [37]. These unique features have enabled microalgae to serve as a versatile platform for O_2 supply to hypoxia organs, such as the brain, heart, pancreas, kidney, and skin [38–43]. In addition, microalgae can be integrated with various materials to augment the inherent photosynthetic capability, such as carbon nanotubes, light-harvesting polymers, and gold nanoparticles [44–47]. Besides, the integration of other synthetic materials can also endow the microalgae with new functions, including extreme environmental tolerance, movement capability, and drug delivery [48–51]. These advantages demonstrate that microalgae have great potential as a universal platform for fabricating living biohybrids with photosynthetic capability and customized integrated functions, especially for tumor hypoxia alleviation.

Here, we present a photothermal microalgae system (PTA) design that synergizes microalgal photosynthetic oxygenation with photothermal therapy (PTT) to boost cancer immunotherapy (Fig. 1). The PTA is constructed by coating microalgae *Chlorella sorokiniana (C. soro)* with a photothermal agent polydopamine (PDA) to form a biohybrid structure. After intratumoral injection, the PTA can alleviate tumor hypoxia by supplying O_2 under 660 nm laser irradiation, which reshapes the TME by targeting the hypoxia-adenosine axis, thereby reversing it from an immunosuppressive state to an immunopermissive state. In addition, this reshaped TME remarkably boosts the antitumor immunity induced by PTT under 808 nm laser irradiation, resulting in significant tumor inhibition. Collectively, this work establishes a PDA-armed microalgal oxygenerator with integrated photosynthetic and photothermal capability to reshape the immunosuppressive TME and boost cancer photothermal immunotherapy.

Results and discussion

Preparation and characterization of PTA

C. soro is a type of eukaryotic green microalgae with a spherical morphology [52]. When excited with appropriate light, *C. soro* can exhibit red autofluorescence owing to the presence of photosynthetic pigments in its body (Figs. S1 and S2). As a photoautotrophic microorganism, *C. soro* possesses the inherent capability to generate O_2 via photosynthesis under both 660 nm and white light irradiation (Fig. S3). Thus, *C. soro* was chosen as a natural living oxygenerator for the preparation of PTA, which involved coating *C. soro* with PDA through in situ polymerization of dopamine. Although PDA provides PTA with photothermal capability, excessive coating may negatively affect microalgal photosynthesis as PDA can reflect and absorb light. To determine the optimal coating content of PDA, we constructed PTA10, PTA20, PTA40, and PTA60 by controlling the reaction time. PDA absorbs broadly over wavelengths ranging from 400 nm to 900 nm, causing the color of microalgal solutions to deepen gradually with increasing reaction time (Fig. 2a and Fig. S4). The optical absorbance of PTA increased while fluorescence intensity decreased correspondingly (Fig. 2b and Fig. S5), confirming the successful coating of *C. soro* with PDA.

As expected, the amount of photosynthetic O_2 produced by microalgae decreased with increasing PDA deposition on *C. soro* (Fig. 2c). Conversely, the heating efficacy of PTA increased with the amount of PDA coated on *C. soro* owing to PDA's photothermal capability (Fig. 2d, e). Therefore, to strike a balance between optimal photosynthetic oxygenation and robust photothermal capability, PTA20 (hereafter referred to as PTA) was selected as our intended material for the subsequent experiments. Compared to *C. soro*, transmission electron microscopy (TEM) revealed that the surface of PTA was much rougher, suggesting the presence of a PDA layer on the microalgal surface (Fig. 2f and Fig S6). To demonstrate PTA's photothermal capability, we employed an 808 nm laser. The solution of PTA exhibited a rapid temperature increase over time, which further increased with increasing PTA concentration or laser power density (Fig. 2g, h). The standard photothermal agent indocyanine green (ICG) inactivated quickly under 808 nm laser irradiation (Fig. S7). Moreover, PTA exhibited similar photothermal performance during five heating/cooling cycles dispersed in different solutions, indicating exceptional photothermal stability of PTA (Fig. 2i and Fig. S8). Moreover, the photothermal conversion efficiency was calculated as 16.24 %, which was sufficient for photothermal therapy. Collectively, these data confirmed the successful construction of PTA with excellent photosynthetic and photothermal capability.

In vitro hypoxia alleviation and immune activation by PTA

To investigate the ability of PTA to alleviate hypoxia in vitro, we characterized its photosynthetic oxygenation. Hypoxia induces the upregulation of HIF-1α, which further drives the overexpression of CD39 and CD73 [1,5]. Therefore, we hypothesized that alleviating hypoxia would inhibit the upregulation of HIF-1α, thereby diminishing the overexpression of CD39 and CD73. We employed immunofluorescence staining to detect changes in the expression of HIF-1α, CD39, and CD73, which are induced by hypoxia. Under normoxic conditions, 4T1 cells showed only slight fluorescence for HIF-1α, CD39, and CD73, while distinct fluorescence emerged after hypoxia incubation. However, co-culturing with PTA under light irradiation resulted in the disappearance of fluorescence, indicating the hypoxia alleviation

Please cite this article in press as: C. Zhang et al., Materials Today (2024), https://doi.org/10.1016/j.mattod.2024.04.001

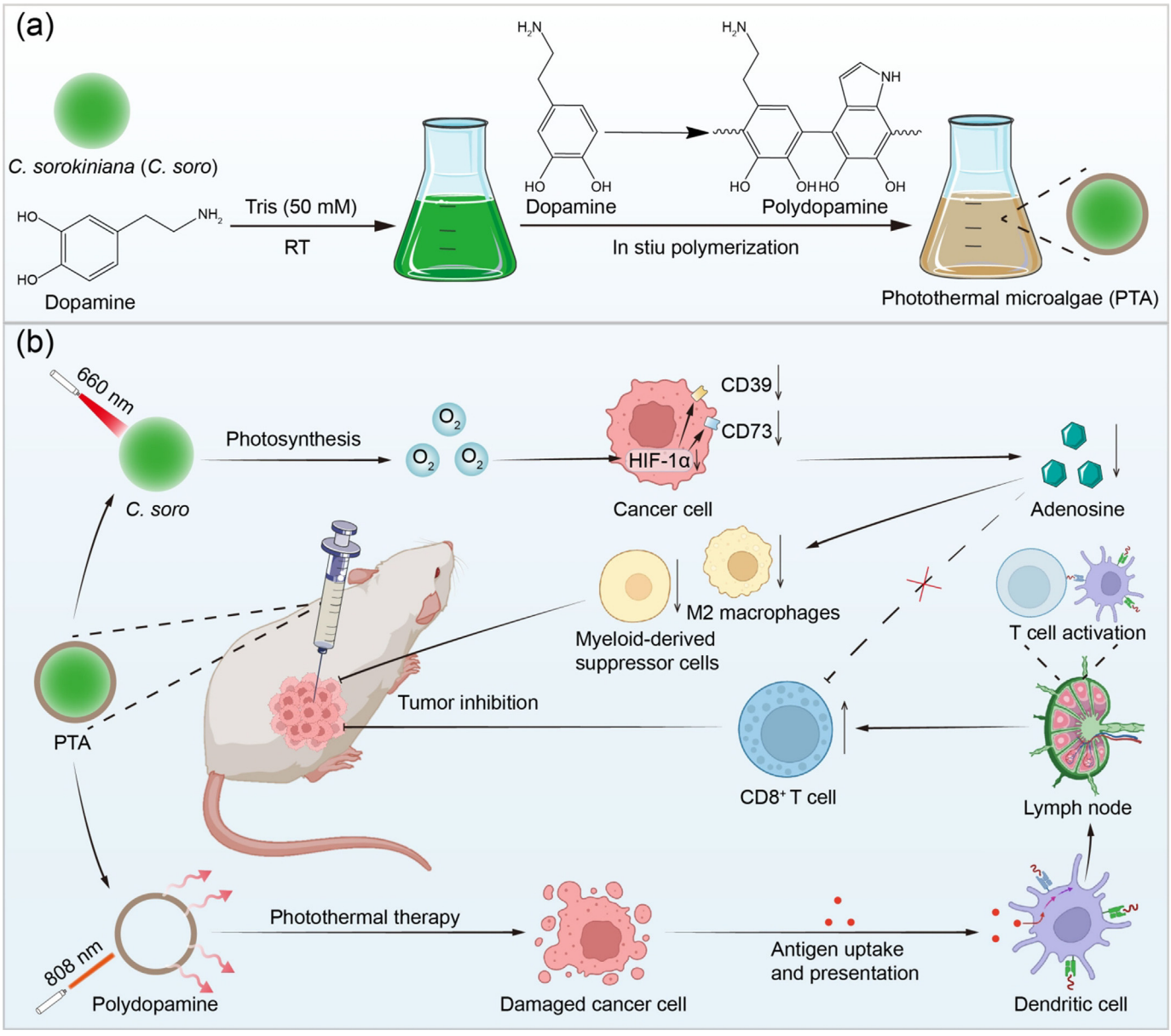

FIG. 1

Schematic representation of PTA-mediated alleviation of tumor hypoxia to reshape the TME and enhance antitumor immune activation. (a) Polymerization of dopamine on the surface of *C. soro* for the construction of PTA. (b) PTA performs photosynthesis to generate oxygen (O_2) upon 660 nm laser irradiation, targeting the hypoxia-adenosine axis and reducing the presence of myeloid-derived suppressor cells and M2 macrophages, thereby weakening immunosuppression within the TME. Additionally, the reshaped TME further enhances the antitumor immunity triggered by PTA-mediated photothermal therapy (PTT) under 808 nm laser irradiation, resulting in a significant inhibition of tumor growth.

effect of PTA through photosynthetic oxygenation (Fig. 3a–c). We also observed that hypoxia treatment increased the adenosine level in 4T1 culture supernatant compared to normoxia treatment, while PTA treatment with light irradiation reverted this situation (Fig. 3d).

Moreover, carboxyfluorescein succinimidyl ester (CFSE) dilution assay was used to monitor the proliferation of T cells in vitro. Compared with the PBS group, adenosine significantly suppressed the proliferation of T cells. However, when cocultured with adenosine and an adenosine receptor inhibitor, ZM241385, the inhibition effect of adenosine on T cells disappeared, confirming the inhibition role of adenosine on T cells (Fig. S9). These results demonstrate that PTA can alleviate cellular hypoxia through photosynthetic oxygenation and downregulate the generation of immunosuppressive adenosine in vitro, which may hold promise for relieving the suppression of T cells.

To evaluate the PTT capability of PTA, we assessed the cell viability of 4T1 cells after different treatments. The PTA and 808 groups exhibited negligible cell viability loss. However, the cell viability decreased significantly in the PTA + 808 group (Fig. 3e). We also verified the PTT killing efficacy on 4T1 cells using the live and dead cell staining assay. Consistent with the quantitative detection of cell viability, only the PTA + 808 group showed obvious red fluorescence from dead cells (Fig. S10). Previous studies have shown that

Please cite this article in press as: C. Zhang et al., Materials Today (2024), https://doi.org/10.1016/j.mattod.2024.04.001

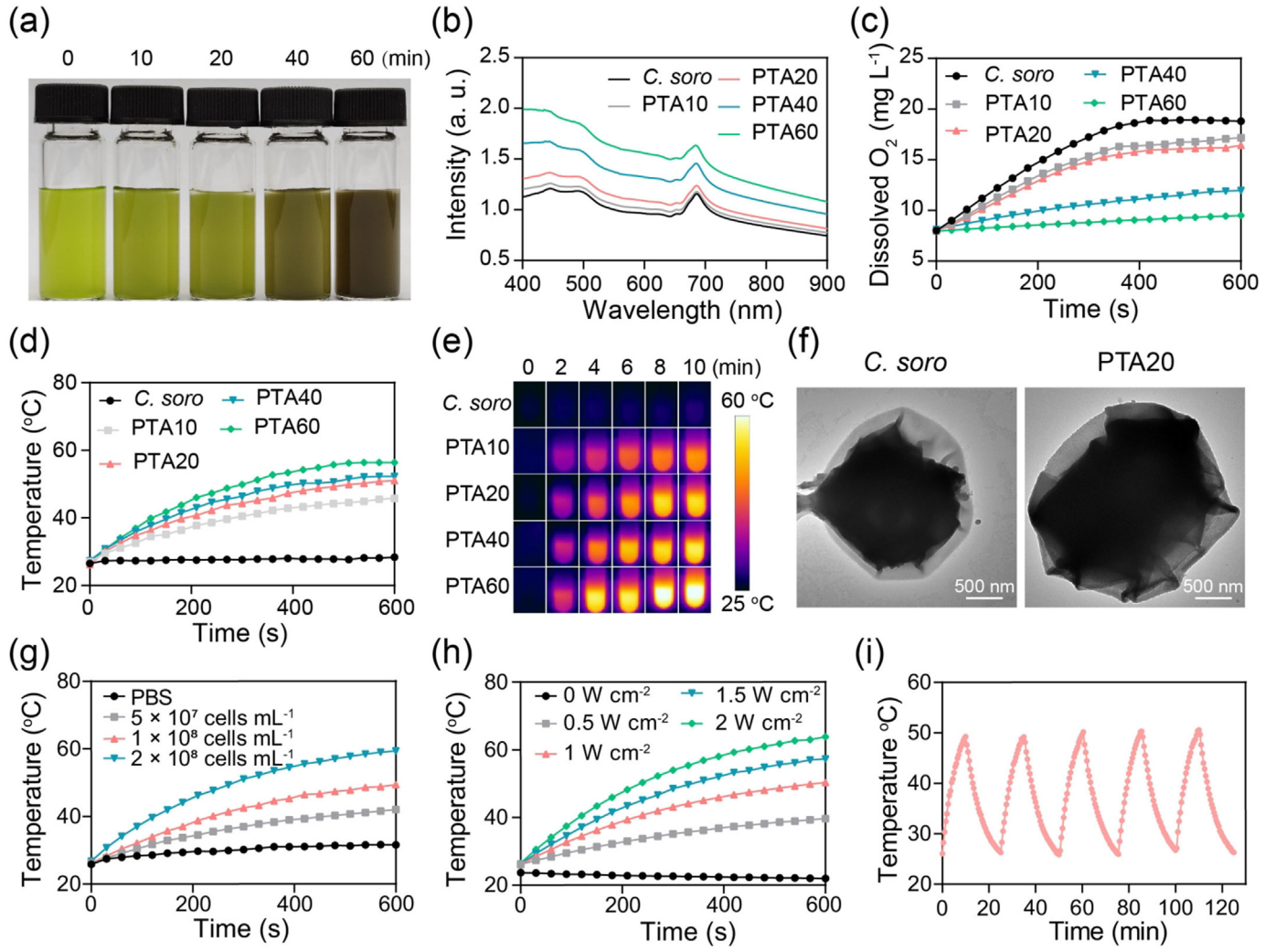

FIG. 2

Preparation and characterization of PTA. (a) Photographs of *C. soro* coated by PDA with different degrees controlled by reaction time. (b) UV–vis spectra of *C. soro*, PTA10, PTA20, PTA40, and PTA60. (c) Dissolved O_2 concentration changes of *C. soro*, PTA10, PTA20, PTA40, and PTA60 at 1×10^8 cells mL^{-1} under 660 nm laser irradiation (10 min, 30 mW cm^{-2}). (d) Photothermal temperature profiles and (e) corresponding thermal images of *C. soro*, PTA10, PTA20, PTA40, and PTA60 at 1×10^8 cells mL^{-1} after 808 nm laser irradiation (10 min, 1 W cm^{-2}). (f) TEM images of *C. soro* and PTA20. (g) Photothermal temperature profiles of PTA20 at different concentrations with 808 nm laser irradiation (10 min, 1 W cm^{-2}). (h) Photothermal temperature profiles of PTA20 (1×10^8 cells mL^{-1}) under different 808 nm laser irradiation power densities. (i) Photothermal stability of PTA20 (1×10^8 cells mL^{-1}) during five heating/cooling cycles dispersed in PBS (808 nm, 10 min, 1 W cm^{-2}).

PTT can induce immunogenic cell death (ICD) [17]. We therefore investigated four hallmarks of ICD, calreticulin (CRT), heat shock protein 70 (HSP-70), heat shock protein 90 (HSP-90), and ATP release in 4T1 cells after various treatments. Flow cytometry analysis verified that only PTA + 808 treatment induced CRT, HSP-70, and HSP-90 exposure in 4T1 cells (Fig. 3f, g and Fig. S11). Immunofluorescence staining for CRT also exhibited superior fluorescence in the PTA + 808 group (Fig. S12). The ATP released from 4T1 cells into the supernatant of the PTA + 808 group was detected as 5-fold higher than the PBS group (Fig. 3h). Furthermore, we examined the potential of PTA-mediated PTT for immune activation by eliciting bone marrow dendritic cells (BMDCs) maturation. As expected, the supernatant of 4T1 cells treated with PTA + 808 induced the highest BMDCs maturation compared to other groups, more than 2-fold compared to the control group (Fig. 3i, j). Additionally, the cytokines TNF-α and IL-6 secreted by BMDCs markedly increased after incubating with the supernatant of 4T1 cells treated with PTA + 808 (Fig. 3k, l). These results confirmed that PTA-mediated PTT successfully induced ICD in 4T1 cells and subsequently promoted the maturation of BMDCs.

The in vitro biosafety of microalgae was evaluated using a hemolysis assay with red blood cells collected from BALB/c mice. The results showed negligible hemolysis in both PTA and *C. soro* treated groups with various concentrations (Fig. S13). Additionally, 3T3 cells and 4T1 cells were treated with various concentrations of PTA or *C. soro* for 24 h without laser irradiation, and no significant cytotoxicity was observed (Fig. S14). These data collectively indicate the satisfactory biocompatibility of *C. soro* and PTA in vitro.

In vivo photosynthetic oxygenation and photothermal capability of PTA

To evaluate the hypoxia-alleviating effect of PTA through photosynthetic oxygenation, we utilized a photoacoustic (PA) imaging

Please cite this article in press as: C. Zhang et al., Materials Today (2024), https://doi.org/10.1016/j.mattod.2024.04.001

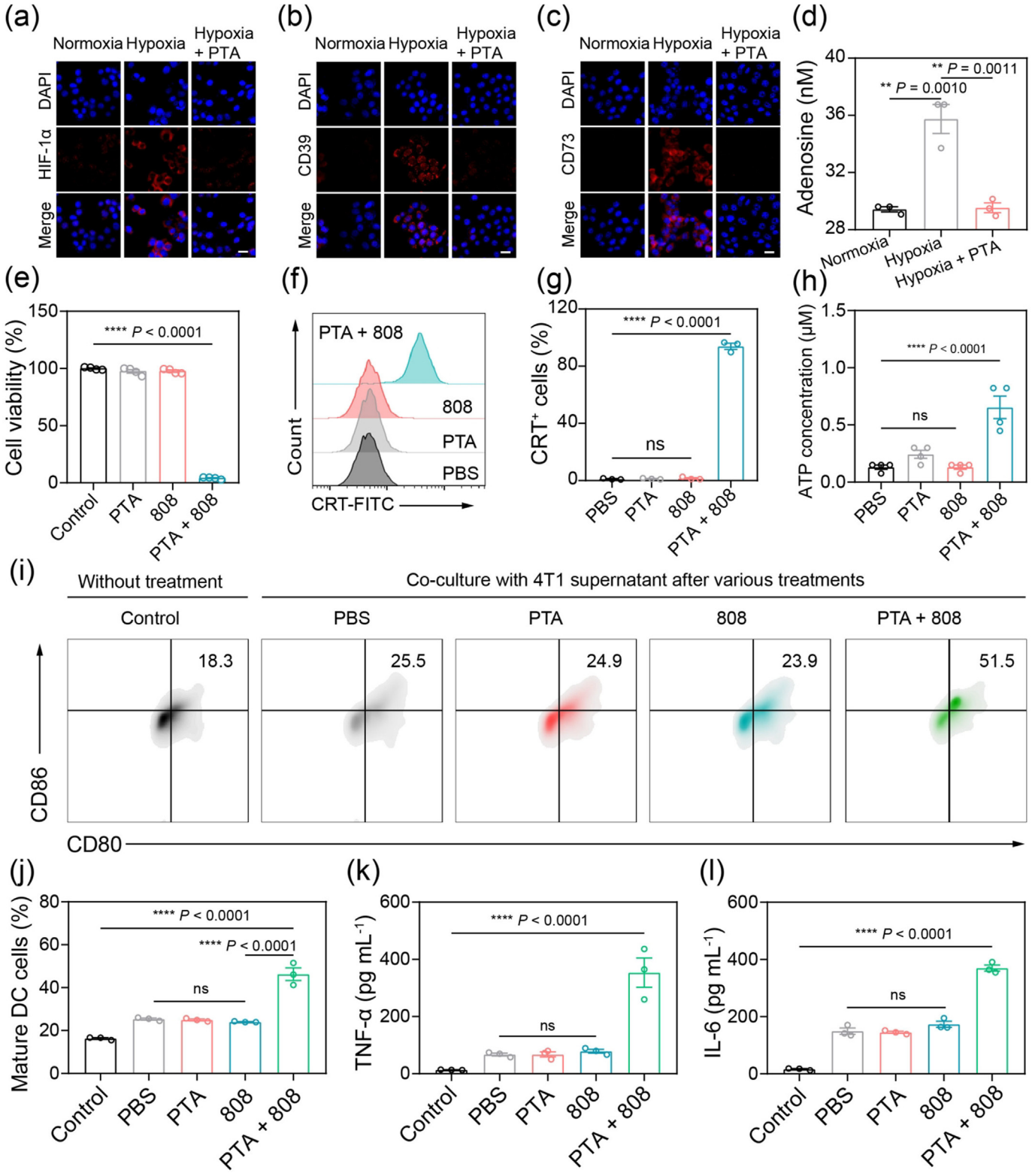

FIG. 3

***In vitro* hypoxia alleviation and immune activation by PTA.** Fluorescence images of (a) HIF-1α in 4T1 cells, (b) CD39 in 4T1 cells, and (c) CD73 in 4T1 cells after different treatments. Scale bar, 20 μm. (d) Extracellular adenosine levels in supernatants of 4T1 cells after various treatments (n = 3). An LED light was employed as the light source in the hypoxia incubator for (a-d). (e) Cell viability of 4T1 cells after different treatments (n = 4). (f) Flow cytometry analysis of CRT and (g) corresponding quantification of CRT-positive cells after various treatments (n = 3). (h) The ATP levels in supernatants of 4T1 cells after various treatments (n = 4). (i) Representative flow cytometry images and (j) corresponding quantification of mature BMDCs ($CD11c^+CD80^+CD86^+$) after various treatments (n = 3). ELISA analysis results of (k) TNF-α and (l) IL-6 in supernatants of BMDCs after different treatments (n = 3). Data are shown as mean values ± SEM. Statistical significance was calculated in (d, e, g, h, j, k, and l) using one-way ANOVA with Tukey post-hoc analysis. $^{**}P < 0.01$, $^{***}P < 0.001$, $^{****}P < 0.0001$. ns, no significance.

Please cite this article in press as: C. Zhang et al., Materials Today (2024), https://doi.org/10.1016/j.mattod.2024.04.001

system for in vivo experiments. By combining ultrasonography (US) imaging to identify tumors and PA imaging to measure the saturation level of O_2 (sO_2) based on the PA effect of oxygenated hemoglobin, we monitored the oxygen levels within the TME following intratumoral injection of PTA. Prior to 660 nm laser irradiation for photosynthetic oxygenation, the average sO_2 detected was only 7.9 %, indicating a hypoxic environment in the tumor tissues. However, after 660 nm laser irradiation, the PA signals from oxygenated hemoglobin in the tumor significantly increased, maintaining an average sO_2 level over 30 % within the initial 2 h (Fig. 4a, b). Moreover, we performed immunofluorescence staining to examine the expression of HIF-1α, CD39, and CD73 at the tumor sites. Consistent with the in vitro results showing downregulation of HIF-1α, CD39, and CD73 through hypoxia alleviation via photosynthetic oxygenation of PTA, these markers were similarly downregulated in vivo (Fig. 4c). Additionally, the concentration of immunosuppressive adenosine within the tumors was significantly reduced in the PTA + 660 group compared to the PBS group (Fig. 4d). Together, these findings provide evidence that PTA can alleviate tumor hypoxia through photosynthetic oxygenation and reduce the production of immunosuppressive adenosine.

Subsequently, the photothermal capability of PTA was investigated in vivo following intratumoral injection. As the low power density of 660 nm laser irradiation on PTA exhibited nearly no photothermal heating in vitro (Fig. S15), we evaluated the photothermal capability of PTA using 808 nm laser irradiation. Among the control group and the 808 group, only the PTA + 808 group exhibited a noticeable temperature increase within the tumor, reaching temperatures exceeding 45 °C within

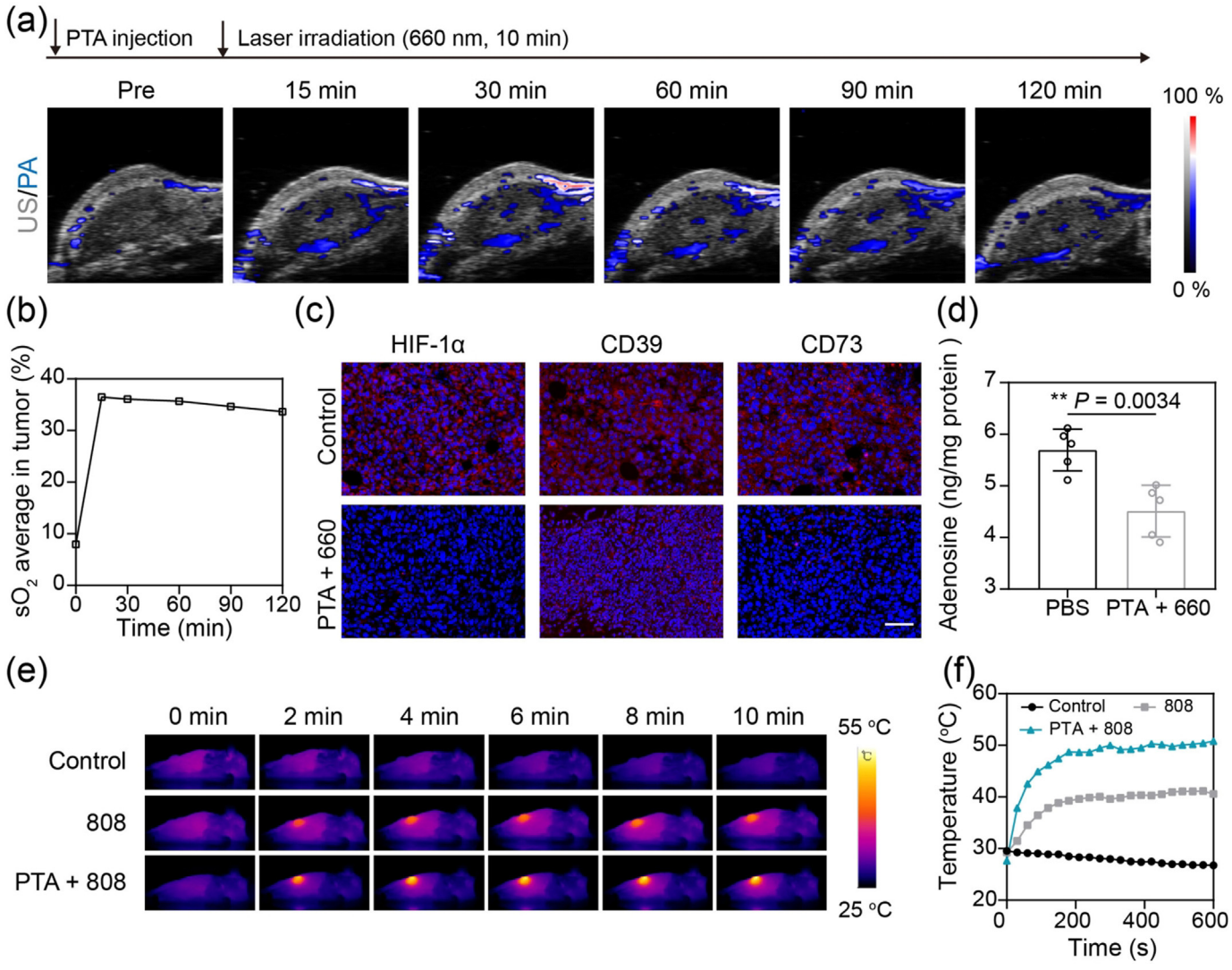

FIG. 4

***In vivo* photosynthetic oxygenation and photothermal capability of PTA.** (a) US/PA images of oxyhemoglobin in 4T1 tumor before and after irradiation with a 660 nm laser, and (b) the corresponding percentages of tissue oxygen saturation (sO_2) calculated from the PA signals. (c) Immunofluorescence staining for HIF-1α, CD39, and CD73 in 4T1 tumor slices after different treatments. Scale bar, 50 μm. (d) Intratumoral adenosine concentrations within 4T1 tumors after different treatments (n = 5). (e) Thermal photographs and (f) corresponding photothermal heating profiles of mice after intratumoral injection of PTA, followed by 808 nm laser irradiation (10 min, 1 W cm^{-2}). Data are presented as mean values ± SEM. Statistical significance was determined in (d) using a two-tailed unpaired Student's t-test. $^{**}P < 0.01$.

Please cite this article in press as: C. Zhang et al., Materials Today (2024), https://doi.org/10.1016/j.mattod.2024.04.001

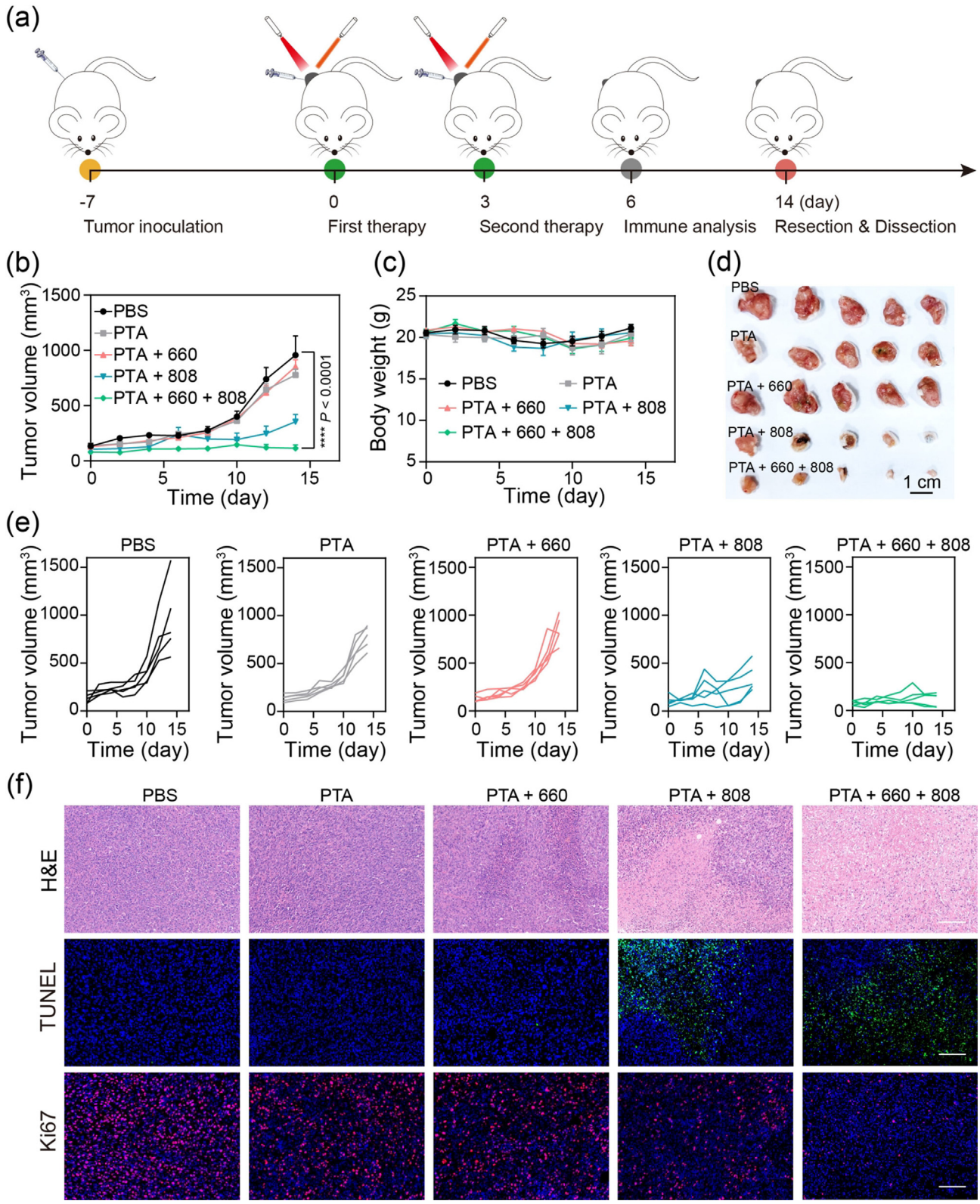

FIG. 5

***In vivo* antitumor capability of PTA-based therapy.** (a) Schematic illustration depicting the therapeutic plan for subcutaneous mouse 4T1 tumors. (b) Tumor growth curves with different treatments ($n = 5$). (c) Mice body weights with different treatments ($n = 5$). (d) Tumor photographs at the end of therapy after different treatments ($n = 5$). (e) Individual tumor growth curves for each mouse in all treatment groups. (f) Tumor histological analysis including H&E, TUNEL, and Ki67 staining after different treatments. Scale bar, 100 μm. Data are presented as mean values ± SEM. Statistical significance was calculated in (b) using one-way analysis of variance (ANOVA) with Tukey's post-hoc analysis. ****$P < 0.0001$.

Please cite this article in press as: C. Zhang et al., Materials Today (2024), https://doi.org/10.1016/j.mattod.2024.04.001

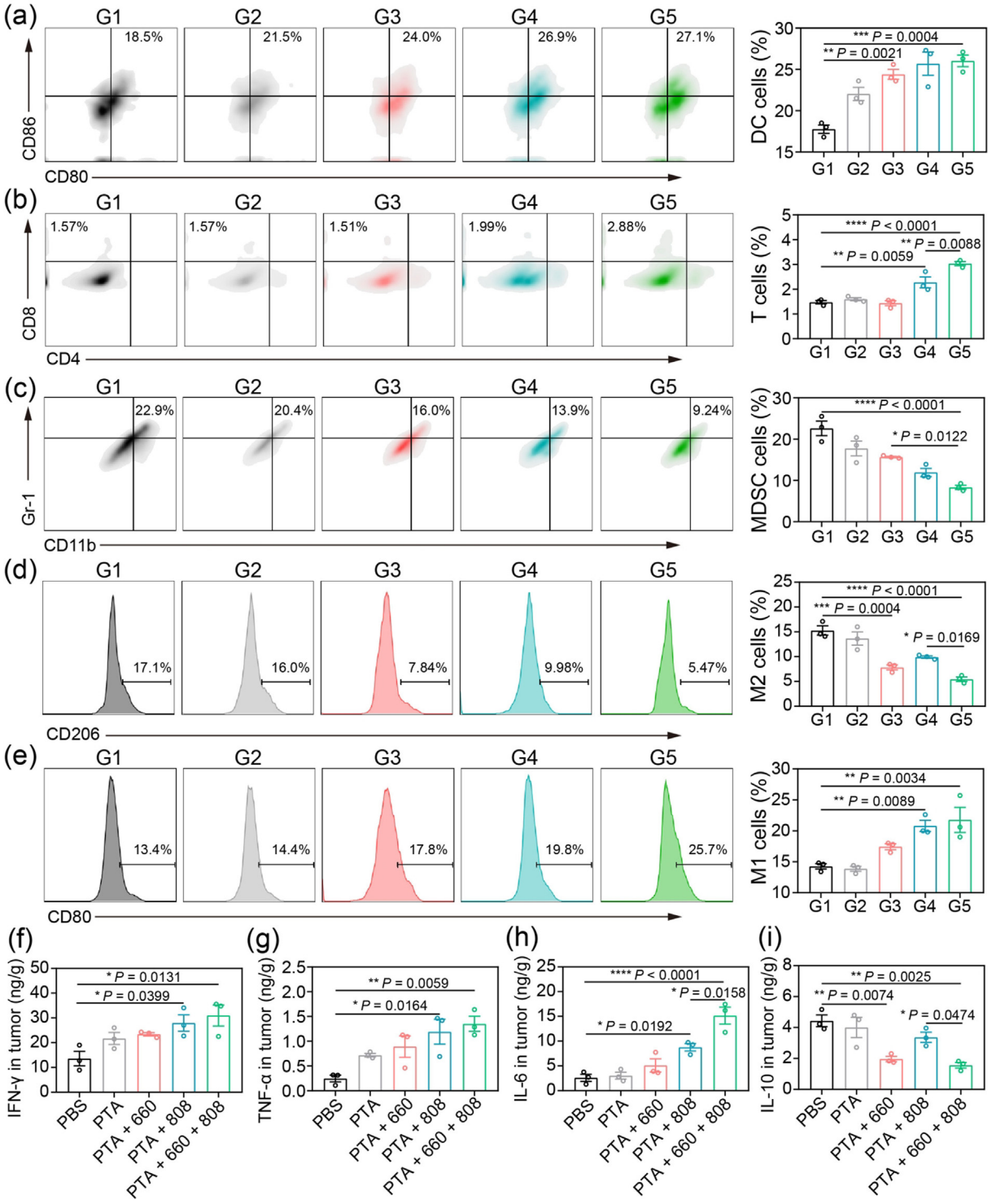

FIG. 6

***In vivo* antitumor immunity mediated by PTA-based therapy.** (a) The mature of $CD80^+CD86^+$ DCs gated on $CD11c^+$ cells within the tumor-draining lymph nodes ($n = 3$). (b) The cytotoxic $CD8^+$ T cells gated on $CD3^+$ cells within tumors ($n = 3$). (c) The level of $CD11b^+Gr\text{-}1^+$ MDSCs gated on $CD45^+$ cells ($n = 3$). (d) TAMs of M2 phenotype highly expressed CD206 gated on $F4/80^+$ cells within tumors ($n = 3$). (e). TAMs of M1 phenotype highly expressed CD80 gated on $F4/80^+$ cells within tumors ($n = 3$). Cytokines of (f) IFN-γ, (g) TNF-α, (h) IL-6 and (i) IL-10 within tumors ($n = 3$). Tumors were collected at the sixth day for flow cytometric analysis after different treatments. Representative flow cytometric analysis images (left) and relative quantification analysis (right) of immune cells as shown. G1, PBS; G2, PTA; G3, PTA + 660; G4, PTA + 808; G5, PTA + 660 + 808. Data are shown as mean values ± SEM. Statistical significance was calculated in (a-i) using one-way ANOVA with Tukey post-hoc analysis. $^*P < 0.05$, $^{**}P < 0.01$, $^{***}P < 0.001$, $^{****}P < 0.0001$.

Please cite this article in press as: C. Zhang et al., Materials Today (2024), https://doi.org/10.1016/j.mattod.2024.04.001

the initial 2 min (Fig. 4e, f). These results demonstrate the excellent photothermal capability of PTA in vivo.

In vivo antitumor efficacy of PTA-based therapy

Motivated by the significant hypoxia alleviation and potent photothermal effect of PTA observed in vivo, we proceeded to evaluate the antitumor potential of PTA using a subcutaneous 4T1 tumor model (Fig. 5a). The mice bearing 4T1 tumors were randomly divided into five groups and subjected to different treatments: (1) PBS, (2) PTA, (3) PTA + 660, (4) PTA + 808, and (5) PTA + 660 + 808. Compared to the PBS group, neither PTA nor PTA + 660 exhibited any suppression of tumor growth, while significant tumor inhibition was observed in the PTA + 808 and PTA + 660 + 808 groups (Fig. 5b, e). Tumor digital images were captured, and tumor weights were measured at the end of the therapy. Consistent with the tumor volume results, noticeable tumor regression was only observed in the groups treated with PTT. Among these groups, the PTA + 660 + 808 group displayed the smallest tumors, indicating a synergistic antitumor effect of photosynthetic oxygenation and PTT (Fig. 5d and Fig. S16). To investigate the antitumor mechanism, tumor tissues were analyzed using histological hematoxylin and eosin (H&E) staining, as well as terminal deoxynucleotidyl transferase dUTP nick end labeling (TUNEL) and Ki67 immunofluorescence staining. H&E and TUNEL staining clearly revealed the largest areas of necrosis and apoptosis in tumor cells in the PTA + 660 + 808 group. Additionally, the mice treated with PTA + 660 + 808 showed reduced tumor proliferation, as indicated by diminished Ki67 immunofluorescence staining (Fig. 5f). Furthermore, the survival rates of the PTA + 808 and PTA + 660 + 808 groups were significantly improved (Fig. S17). These findings demonstrate the remarkable antitumor efficacy of PTA-based therapy, combining photosynthetic oxygenation and PTT.

Throughout the course of therapy, the body weight of the mice remained relatively stable across all treatment groups (Fig. 5c). After a two-week treatment period, blood and major organs were collected for analysis. No significant alterations were observed in blood biochemistry or blood routine indexes following various treatments (Fig. S18). Furthermore, two markers of systemic inflammation and infection, C-reactive protein (CRP) and procalcitonin (PCT), were examined in mouse serum, and no significant differences were found among the groups (Fig. S19). Moreover, histological H&E staining of the major organs from mice treated with different therapies revealed normal morphology (Fig. S20). Collectively, these data indicate that PTA-based therapy exhibits satisfactory biosafety.

In vivo antitumor immunity mediated by PTA-based therapy

To investigate the immune activation mechanism induced by PTA-based therapy, we evaluated the occurrence of ICD within tumors after various treatments. The exposure of CRT, HSP-70, and HSP-90 within tumors significantly increased in the PTA + 660 and PTA + 660 + 808 groups compared to other groups (Fig. S21). We then examined immune cells in tumor-draining lymph nodes (TDLNs) and tumor tissues using flow cytometry after various treatments. The PTA + 660 + 808 group exhibited a significant increase in the percentage of mature dendritic cells (DCs) in TDLNs, reaching 26.0 %, surpassing the PBS group at 17.8 %. By contrast, the PTA, PTA + 660, and PTA + 808 groups showed DC maturation ratios of 22.0 %, 24.4 %, and 25.7 %, respectively (Fig. 6a). Moreover, cytotoxic $CD8^+$ T cells within tumors were assessed for their potent antitumor efficacy. The percentage of $CD8^+$ T cells within tumors treated with PTA + 808 and PTA + 660 + 808 was 1.55-fold and 2.06-fold higher than that in the PBS group, respectively. However, PTA and PTA + 660 groups had little influence on $CD8^+$ T cells (Fig. 6b).

Furthermore, immunosuppressive immune cells, including MDSCs and M2 macrophages, were both downregulated in the PTA + 660 group relative to the PBS group, indicating the weakening of immunosuppression in the TME through hypoxia alleviation. The percentage of MDSCs and M2 macrophages was further reduced in the PTA + 660 + 808 group, demonstrating a synergistic effect between photosynthetic oxygenation and PTT (Fig. 6c, d). The downregulation of M2 macrophages may have been accompanied by the upregulation of antitumor M1 macrophages, as M1 and M2 macrophages can polarize from one phenotype to the other in the TME. Specifically, the percentage of M1 macrophages significantly increased in the PTA + 808 and PTA + 660 + 808 groups (Fig. 6e). Moreover, the ratio of M1/M2 also remarkably increased in the PTA + 660 + 808 group, reaching 4.26-fold higher than that in the PBS group, indicating that the M2 macrophages polarized to the M1 macrophages in the TME after combination treatment with photosynthetic oxygenation and PTT (Fig. S22). Additionally, proinflammatory cytokines such as IFN-γ, TNF-α, and IL-6 were significantly increased in the PTA + 660 + 808 group (Fig. 6f–h). Conversely, the involvement of immunosuppressive MDSCs and M2 macrophages in the anti-inflammatory cytokine IL-10 was decreased in the PTA + 660 and PTA + 660 + 808 groups (Fig. 6i). These results suggest that PTA-based therapy could reshape the TME to boost anticancer efficacy by decreasing protumor immune cells and anti-inflammatory cytokines while increasing antitumor immune cells and proinflammatory cytokines.

Transcriptomic analysis of the anticancer mechanism mediated by PTA-based therapy

The anticancer mechanism of PTA + 660 + 808 in 4T1 tumor-bearing mice was analyzed comprehensively using transcriptomics. The total number of detected genes showed significant differences between the PBS and PTA + 660 + 808 groups (Fig. 7a). Specifically, 5185 genes were upregulated and 2017 genes were downregulated in the PTA + 660 + 808 group compared to the PBS group (P-value < 0.05 and fold change ≥2) (Fig. 7b). Gene ontology (GO) analysis revealed that the differentially expressed genes related to immunity were mainly associated with gamma-delta T cell activation, macrophage chemotaxis, dendritic cell differentiation, and negative regulation of interleukin-10 production (Fig. 7d). These pathways indicate the activation of antitumor immune cells and downregulation of the anti-inflammatory cytokine IL-10. Additionally, PTA + 660 + 808 significantly upregulated proinflammatory genes (e.g., *Tnfsf15*, *Ifngr1*, *Il1a*, *Il12a*, *Il18r1*, and *Il36g*),

Please cite this article in press as: C. Zhang et al., Materials Today (2024), https://doi.org/10.1016/j.mattod.2024.04.001

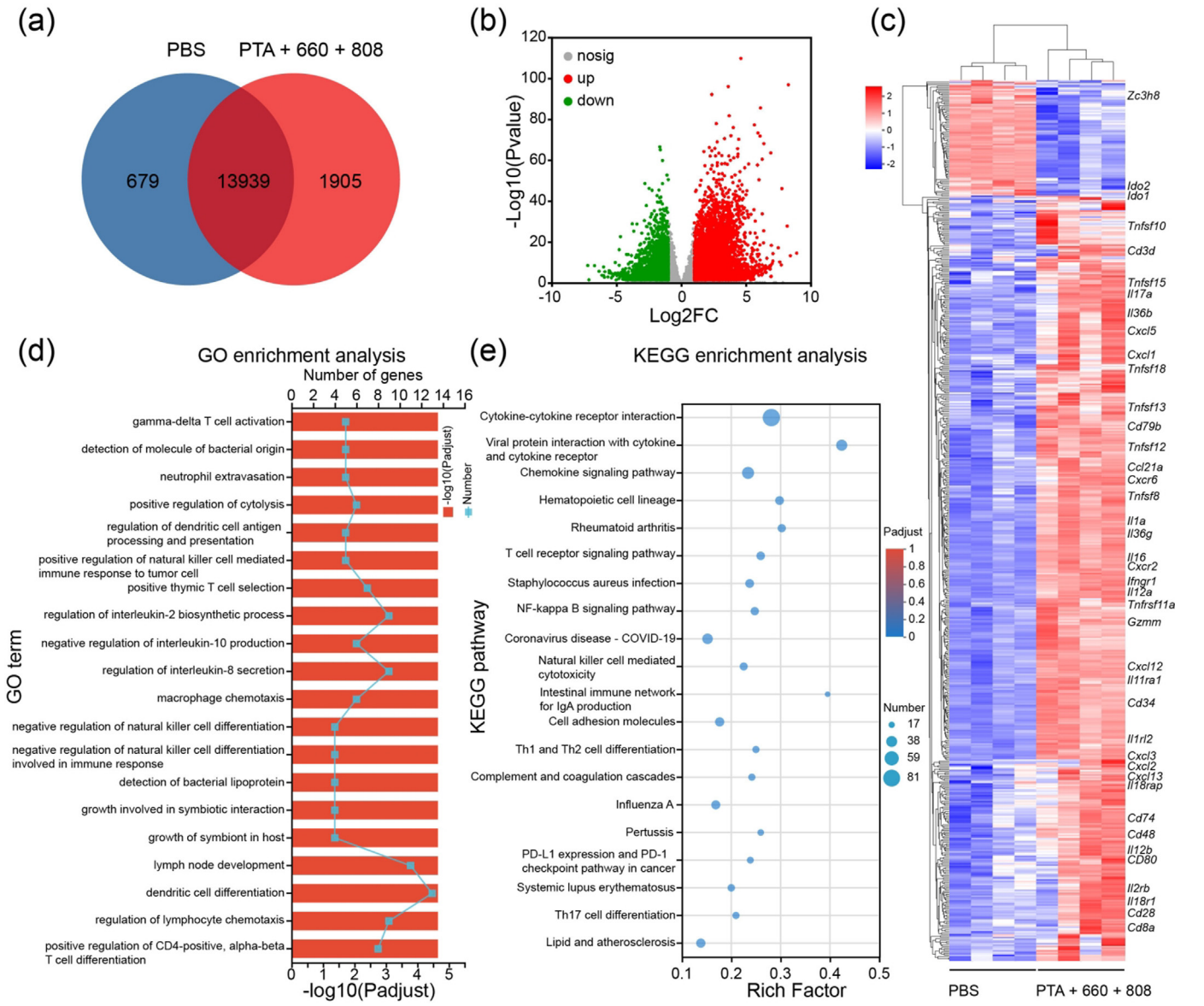

FIG. 7

Transcriptomic analysis for the anticancer mechanism of PTA-based therapy. (a) Venn diagram of detected genes in 4T1 tumors treated with PBS and PTA + 660 + 808. (b) Volcano plot of fold changes of the genes identified at $q < 0.05$. (c) Heat map of the representative upregulated and downregulated genes in 4T1 tumors after PBS and PTA + 660 + 808 treatments. (d) GO enrichment analysis of immune system process related top 20 genes of the PTA + 660 + 808 group compared to the PBS group. (e) KEGG enrichment analysis of immune-related top 20 pathways after treated with PBS and PTA + 660 + 808.

immune cell-recruiting genes (e.g., *Cxcl1*, *Cxcl2*, *Cxcl3*, *Cxcl5*, *Ccl21a*, and *Il-16*), and lymphocyte activation genes (*Gzmm*, *Cd3d*, *Cd8a*, *Cd28*, *Cd48*, and *Cd80*). Conversely, the downregulated genes *Zc3h8*, *Ido1*, and *Ido2*, which suppress the activation of antitumor immunity, also suggest that PTA + 660 + 808 successfully attenuated immunosuppression in the TME (Fig. 7c). Analysis of immune-related genes in the Kyoto Encyclopedia of Genes and Genomes (KEGG) pathways revealed their association with multiple immune activation pathways, including cytokine-cytokine receptor interaction, chemokine signaling pathway, T cell receptor signaling pathway, and NF-kappa B signaling pathway (Fig. 7e). In summary, these comprehensive transcriptomic results suggest that PTA + 660 + 808 could attenuate immunosuppression in the TME, recruit immune cells, and activate T lymphocytes to induce robust antitumor immunity.

Conclusions

By utilizing the natural microalgae *C. soro*, we developed a PDA-armed microalgal oxygenerator named PTA to counteract the hypoxia-induced immunosuppression in the TME and enhance PTT-induced antitumor immune responses. Through the photosynthetic process of PTA, in situ O_2 generation within the tumor was achieved, effectively alleviating hypoxia and subsequently downregulating the immunosuppressive molecule adenosine, thus addressing the core of the hypoxia-adenosine axis. In a sub-

Please cite this article in press as: C. Zhang et al., Materials Today (2024), https://doi.org/10.1016/j.mattod.2024.04.001

cutaneous 4T1 mouse model, this reoxygenation process significantly reduced the proportion of MDSCs and M2 macrophages, thereby attenuating immunosuppression in the TME. Furthermore, due to the reshaped immunopermissive TME, PTA-based PTT induced stronger antitumor immune responses, leading to enhanced inhibition of tumor growth. This study demonstrates the potential of in situ O_2 generation within the tumor using living microalgae to reshape the immunosuppressive TME and enhance hypoxia-constrained antitumor immunity.

Experimental section

Materials

Dopamine hydrochloride (CAS: 62-31-7) was purchased from Shanghai Meryer Biochemical Technology Co., LTD. Tris (CAS: 77-86-1) was obtained from BioFroxx. ICG was obtained from Aladdin Reagents (Shanghai, China). BG11 medium was acquired from Qingdao Hai Bo Biotechnology Co., LTD. Methyl thiazolyl tetrazolium (MTT), recombinant murine IL-2, recombinant murine IL-4, recombinant murine GM-CSF, and CFSE assay kit were purchased from Beyotime Biotechnology Co., Ltd. Dimethyl sulfoxide was purchased from Leyan (Shanghai, China). Cell culture dishes/plates and 20-mm glass-bottom dishes were purchased from NEST Biotechnology co., ltd. Roswell Park Memorial Institute (RPMI) 1640 culture medium was acquired form Sperikon Life Science & Biotechnology co., ltd. Fetal bovine serum (FBS), penicillin, streptomycin, and trypsin were obtained from VivaCell (Shanghai, China). ELISA kits for IFN-γ, TNF-α, IL-6, and IL-10 were purchased from Hangzhou Multisciences Biotechnology Co., LTD. The ELISA kit for adenosine was purchased from Shanghai Coibo Bio Technology Co., LTD. ELISA kits for CRP and PCT were acquired from Wuhan Newqidi Biological Technology Co., Ltd. The ATP content assay kit was obtained from Beijing Solarbio Science & Technology Co., Ltd. Anti-CRT antibody was acquired from StressMarq Biosciences, Inc. Anti-HSP-70 antibody was purchased from Biolegend. Anti-HSP-90 antibody was obtained from Proteintech Group, Inc. ZM241385 was acquired from MedChemExpress (Monmouth Junction, NJ, USA).

Characterization

Scanning electron microscopy (SEM, GeminiSEM 500) and transmission electron microscopy (TEM, JEM-2100) were utilized to observe the morphology of microalgae. UV–vis absorbance spectra were measured using UV–vis spectroscopy (Lambda Bio40). Dissolved O_2 concentrations were recorded using a dissolved oxygen meter (INESA Scientific Instrument Co., Ltd, JPSJ-605F). Temperature changes were monitored using a thermal camera (JIR-A384). Cell viability was assessed using a microplate reader (Bio-Rad, Model 550, USA). Confocal laser scanning microscopy (CLSM, Nikon C1-si TE2000) was employed for confocal microscopy imaging. The 660 nm laser (Beijing STONE laser) and 808 nm laser (Hi-Tech optoelectronics Co., Ltd, LOS-BLD-0808-005W) were used for photosynthetic oxygenation and photothermal performance. Blood samples were analyzed for blood routine (MC-6200VET) and blood biochemistry (MNCHIP, Tianjin, China). Flow cytometry data were collected using a flow cytometer (BD FACS Aria III, USA) and analyzed with FlowJo v.10.

Microalgae and cell culture

Chlorella sorokiniana (*C. soro*, FACHB-24) was obtained from the Institute of Hydrobiology, Chinese Academy of Sciences. *C. soro* was cultured in BG11 medium under a 12-hour light/12-hour dark photoperiod at 25 °C. Murine 4T1 breast tumor cells (4T1) were purchased from the China Center for Type Culture Collection (CCTCC). 4T1 cells were incubated in RPMI 1640 medium supplemented with 10 % (v/v) fetal bovine serum (FBS) and 1 % (w/v) penicillin (100 U mL^{-1})/streptomycin (100 μg mL^{-1}) under normoxia (21 % O_2) or hypoxia (1 % O_2) with 5 % CO_2 at 37 °C. Bone marrow dendritic cells (BMDCs) were collected from 8-week-old BALB/c mice and cultured in RPMI 1640 (10 % FBS, 100 U mL^{-1} penicillin, and 100 μg mL^{-1} streptomycin) containing IL-4 (10 ng mL^{-1}) and GM-CSF (20 ng mL^{-1}) under normoxia (21 % O_2) with 5 % CO_2 at 37 °C. The medium was replaced on day 3, and the BMDCs were harvested on day 6 for further investigation.

Preparation of PTA

C. soro cells were collected by centrifugation at 6000 rpm for 3 min and washed with ultrapure water three times before being dispersed in Tris buffer solution (50 mM) to a concentration of 1×10^8 cells mL^{-1}. Then, dopamine hydrochloride (3 mg mL^{-1}) was added to this solution and gently stirred at room temperature for 10, 20, 40, and 60 min to obtain PTA10, PTA20, PTA40, and PTA60, respectively. After the reaction, the pellets were collected by centrifugation at 6000 rpm for 3 min and washed with phosphate buffer saline (PBS) three times before proceeding to the subsequent experiments.

Measurement of photosynthetic oxygenation of PTA

The dissolved O_2 concentration was measured using a dissolved oxygen meter. For photosynthetic oxygenation of bare *C. soro*, 30 mL of bare microalgal solution in a 50 mL centrifuge tube was assayed with different concentrations (dispersed in PBS with a concentration of 1×10^7, 5×10^7, and 1×10^8 cells mL^{-1}) or different solutions (1×10^8 cells mL^{-1}C. soro solution dispersed in PBS, H_2O, BG11, and RPMI 1640) under identical 660 nm light intensity (6000 lx) for 10 min. The O_2 production performance of *C. soro* (1×10^8 cells mL^{-1}, dispersed in PBS) under red light (660 nm) or white light (LED light) with identical light intensity (6000 lx) for 10 min was evaluated. For photosynthetic oxygenation of PTA, 30 mL of microalgal solution (1×10^8 cells mL^{-1} of *C. soro*, PTA10, PTA20, PTA40, and PTA60) in a 50 mL centrifuge tube was assayed under 660 nm irradiation (6000 lx) for 10 min.

Photothermal performance of PTA

1 mL of *C. soro*, PTA10, PTA20, PTA40, and PTA60 solution (1×10^8 cells mL^{-1}) was irradiated with an 808 nm laser (1 W cm^{-2}, 10 min). The temperature changes were recorded using a thermal camera. PTA20 (hereafter referred to as PTA) dispersed in PBS was finally selected for investigating the photothermal performance at different concentrations (0, 5×10^7, 1×10^8, and 2×10^8 cells mL^{-1}), different 808 nm laser irradiation powers (0, 0.5, 1, 1.5, 2 W cm^{-2}). The photothermal heating/cooling cycles of PTA were evaluated in PBS, H_2O, BG11, and RPMI-1640, respectively. The photothermal heating/cooling cycles of ICG (18.75 μg mL^{-1} dispersed in PBS) were evaluated under 808 nm

Please cite this article in press as: C. Zhang et al., Materials Today (2024), https://doi.org/10.1016/j.mattod.2024.04.001

laser irradiation (10 min, 1 W cm^{-2}). The photothermal conversion efficiency of the (η) was calculated using the following formula: η (%) = [Cw * ΔT * m/PL * S * t] * 100 %. Cw: heat capacity of water. ΔT: temperature differential of the sample before and after irradiation. m: the mass of the sample. PL: the power density of the laser. S: the area of the irradiated site. t: the irradiation time.

Hemolysis assay

Whole blood from BALB/c mice was collected in citrate-containing tubes. After centrifugation at 5000 rpm for 5 min at 4 °C and washing with PBS five times, the red blood cells were dispersed in PBS for subsequent assays. Fifty microliters of red blood cell solution were added to 450 μl of microalgal solution containing different concentrations of *C. soro* or PTA (1×10^6, 1×10^7, and 1×10^8 cells mL^{-1}). Additionally, 50 μl of red blood cell solution were added to 450 μl of H_2O and PBS as positive and negative controls, respectively. The mixed solutions were then incubated in a shaking water bath at 37 °C and 300 rpm for 30 min. After incubation, the solutions were centrifuged at 5000 rpm for 5 min at 4 °C, and the supernatants were transferred into a 96-well plate for absorbance measurement at 570 nm using a microplate reader. The hemolysis rate was calculated as:

Hemolysis rate (%) = [(sample OD_{570} − negative control OD_{570})/(positive control OD_{570} − negative control OD_{570})] × 100.

In vitro cellular hypoxia alleviation

4T1 cells (2×10^5 per cell) were cultured in 6-well cell culture plates under normoxia (21 % O_2) conditions for 24 h. Afterward, 4T1 cells were subjected to either normoxia (21 % O_2) or hypoxia (1 % O_2) conditions for an additional 4 h. The hypoxia-cultured 4T1 cells were incubated with or without PTA (1 mL per 6-well transwell, 1×10^8 cells mL^{-1}) under constant white light irradiation (LED). The cells were then stained with HIF-1α, CD39, and CD73 antibodies for confocal laser scanning microscopy (CLSM) observation. Additionally, adenosine detection was performed using a mouse adenosine ELISA kit to detect potential changes in adenosine concentrations in the supernatants.

In vitro inhibition of adenosine on T cells

Spleen cells were isolated from the BALB/c mice and stained with a CFSE probe according to the instructions. Then, the spleen cells were cultured in RPMI-1640 supplemented with concanavalin A (2.5 μg mL^{-1}) and IL-2 (100 U mL^{-1}). Adenosine (100 nM) with or without the adenosine receptor inhibitor (ZM241385, 10 nM) was added and further incubated for 72 h. After incubation, the cells were stained with anti-CD3-PE (Biolegend) and analyzed by flow cytometry.

Cytotoxicity assay and ICD induction in vitro

4T1 or 3T3 cells were seeded in 24-well cell culture plates at a density of 5×10^4 cells per well and incubated for 24 h. Then, the 24-well transwell chambers were placed on top, and fresh medium containing various concentrations of *C. soro* or PTA (0, 1×10^6, 5×10^6, 10×10^6, 50×10^6, 100×10^6 cells mL^{-1}) was added (0.1 mL per transwell) and cultured for an additional 24 h. After incubation, cell viability was assessed using the MTT assay. To evaluate photothermal killing, 4T1 cells were seeded in 24-well cell culture plates at a density of 5×10^4 cells per well and incubated for 24 h, and the transwell chambers were placed on top. Fresh medium containing different concentrations of PTA (0, 2.5×10^7, 5×10^7, 1×10^8 cells mL^{-1}) was added (0.1 mL per transwell), followed by irradiation with or without 808 nm laser (1 W cm^{-2}, 10 min). The transwells were then removed and incubated for an additional 8 h. Cytotoxicity was assessed using the MTT assay and Live/Dead cell staining assay. To evaluate immunogenic cell death (ICD) induction, the cells were stained with CRT antibody for CLSM observation. Moreover, flow cytometry analysis was used to quantitatively detect the exposure of CRT, HSP-70, and HSP-90. Furthermore, ATP detection was performed using an ATP content assay kit to analyze supernatant samples.

In vitro BMDC activation

4T1 cells were seeded in 24-well cell culture plates (5×10^4 cells per well) and incubated for 24 h. Then, the 24-well transwell chambers were placed on top, and fresh medium containing PBS or PTA (0.1 mL per transwell, 1×10^8 cells mL^{-1}) was added. After irradiation with or without 808 nm laser (1 W cm^{-2}, 10 min), the transwells were removed and cells were cultured for an additional 8 h. The supernatants were collected and incubated with BMDCs for 24 h. Then, the BMDCs were harvested and stained with anti-CD11c-FITC, anti-CD80-PE and anti-CD86-APC antibodies purchased from Biolegend for flow cytometry analysis.

Animals and 4T1 tumor-bearing mice model

A subcutaneous 4T1 tumor-bearing mice model was established by injecting 1×10^6 4T1 breast tumor cells into the subcutaneous tissue of female BALB/c mice (6–8 weeks). All animal experimental procedures were performed in accordance with the Regulations for the Administration of Affairs Concerning Experimental Animals approved by the State Council of People's Republic of China, and all protocols were approved by the Institutional Animal Care and Use Committee (IACUC) of the Animal Experiment Center of Wuhan University (Wuhan, China).

In vivo photosynthetic oxygenation and hypoxia alleviation

When the tumors reached approximately 150 mm^3, 4T1 tumor-bearing mice were intratumorally injected with PTA (1×10^8 cells mL^{-1}, 100 μL). The intratumoral oxygen level was observed and calculated by photoacoustic imaging (Vevo LAZR imaging system) before and after 660 nm laser irradiation (30 mW cm^{-2}, 10 min). For the analysis of in vivo hypoxia alleviation, PBS (100 μL) or PTA (1×10^8 cells mL^{-1}, 100 μL) was intratumorally injected, followed by 660 nm laser irradiation (30 mW cm^{-2}) for photosynthetic oxygenation when tumors reached approximately 150 mm^3. After 4 h, tumor tissues were collected for immunofluorescence staining of HIF-1α, CD39, and CD73. The collected tumor tissues were homogenized for intratumoral adenosine measurement, and the adenosine in the supernatants was assayed using an adenosine ELISA kit.

Please cite this article in press as: C. Zhang et al., Materials Today (2024), https://doi.org/10.1016/j.mattod.2024.04.001

In vivo photothermal imaging

When the tumors reached approximately 150 mm^3, 4T1 tumor-bearing mice were intratumorally injected with PTA (1×10^8 cells mL^{-1}, 100 μL). Subsequently, 808 nm laser irradiation (1 W cm^{-2}, 10 min) was used for photothermal heating, and the temperature changes of tumors were recorded using a photothermal camera.

Antitumor treatment

One week after tumor inoculation, 4T1 tumor-bearing mice were randomly divided into five groups: (1) PBS; (2) PTA; (3) PTA + 660; (4) PTA + 808; (5) PTA + 660 + 808. PBS (100 μL) and PTA (1×10^8 cells mL^{-1}, 100 μL) were intratumorally administered twice on day 0 and day 3. Then, 660 nm laser irradiation (30 mW cm^{-2}, 10 min) and 808 nm laser irradiation (1 W cm^{-2}, 10 min) were used alone or in combination. The body weight and tumor volume of each mouse were recorded every two days. After 2 weeks of the first treatment, mice were sacrificed, and tumors were excised and collected for H&E, TUNEL, and Ki67 staining. Additionally, blood and major organs of mice were collected for biosafety analysis.

Antitumor immunity analysis

After the various treatments as described above, the mice were sacrificed on day 6. Tumor-draining lymph nodes (TDLNs) and tumors were collected for immune cell analysis using flow cytometry. TDLNs were triturated with 2 % FBS in RPMI 1640, and the cells were collected for flow cytometry analysis after staining with specific antibodies. Tumors were digested with RPMI 1640 medium containing 2 % FBS, 1 mg mL^{-1} collagenase type IV, 0.2 mg mL^{-1} deoxyribonuclease I, and 0.1 mg mL^{-1} hyaluronidase to prepare single-cell suspensions. The tumor single-cell suspensions were collected and stained with specific antibodies for flow cytometry analysis. The antibodies used in flow cytometry were: anti-CD11c-FITC, anti-CD80-PE, and anti-CD86-APC for DCs in TDLNs; anti-CD3-FITC, anti-CD4-APC, and anti-CD8a-PE for $CD8^+$ T cells in tumors; anti-CD45-PE, anti-Gr-1-FITC, and anti-CD11b-APC for MDSCs in tumors; anti-F4/80-APC and anti-CD80-PE for M1 macrophages in tumors; and anti-F4/80-APC and anti-CD206-FITC for M2 macrophages. All antibodies were purchased from Biolegend. The collected tumors were also stained with CRT antibody for CLSM observation. For cytokine detection, tumors were homogenized, and the supernatants were assayed using ELISA kits for IFN-γ, TNF-α, IL-6, and IL-10.

Transcriptomic analysis

Following one week of tumor inoculation, mice were randomly allocated into two groups: (1) PBS; (2) PTA + 660 + 808. Intratumoral injections of PBS (100 μL) and PTA (1×10^8 cells mL^{-1}, 100 μL) were administered twice on day 0 and day 3. Subsequently, the PTA + 660 + 808 group received 660 nm laser irradiation (30 mW cm^{-2}, 10 min) and 808 nm laser irradiation (1 W cm^{-2}, 10 min). On day 6, the mice were euthanized, and the tumors were collected for high-throughput transcriptome sequencing conducted by Majorbio BioTech Co., Ltd.

Data collection and analysis

Statistical analyses were performed using GraphPad Prism 8. The experimental data were presented as means ± SEM. Two-tailed Student's *t*-test was used for statistical analysis of two groups, while one-way ANOVA with Tukey's multiple comparisons test was employed for statistical analysis of multiple groups. A significance threshold of $P < 0.05$ was considered statistically significant for all tests.

Data and materials availability

All data needed to evaluate the conclusions in the paper are present in the paper and/or the Supplementary Materials. Additional data and source files are available from the corresponding author upon reasonable request.

CRediT authorship contribution statement

Cheng Zhang: Conceptualization, Investigation, Writing – original draft. **Zi-Yi Han:** Conceptualization, Investigation, Writing – original draft. **Ke-Wei Chen:** Investigation. **Yu-Zhang Wang:** Investigation. **Xiao Yan:** Investigation. **Xian-Zheng Zhang:** Conceptualization, Funding acquisition, Writing – review & editing, Project administration, Resources, Supervision.

Data availability

Data will be made available on request.

Declaration of competing interest

The authors declare that they have no known competing financial interests or personal relationships that could have appeared to influence the work reported in this paper.

Acknowledgements

This work was supported by the National Natural Science Foundation of China (52333004, 51988102, 22135005) and National Key Research and Development Program of China (2019YFA0905603) and Fundamental Research Funds for the Central Universities of China (2042021kf1014). All animal experiments were conducted under protocols (AUP, WP20210503) approved by the Institutional Animal Care and Use Committee (IACUC) of the Animal Experiment Center of Wuhan University (Wuhan, P. R. China).

Appendix A. Supplementary data

Supplementary data to this article can be found online at https://doi.org/10.1016/j.mattod.2024.04.001.

References

[1] D. Vijayan et al., Nat. Rev. Cancer 17 (2017) 709–724.
[2] X.M. Jing et al., Mol. Cancer 18 (2019) 157.
[3] G.L. Semenza, Semin. Cancer Biol. 96 (2023) 5–10.
[4] S.J. Ma et al., Nat. Commun. 13 (2022) 4118.
[5] S.M. Hatfield et al., J. Mol. Med. 92 (2014) 1283–1292.
[6] D. Boison, G.G. Yegutkin, Cancer Cell 36 (2019) 582–596.
[7] S.M. Hatfield et al., Sci. Transl. Med. 7 (2015) 277ra30.
[8] C. Cekic et al., Cancer Res. 74 (2014) 7250–7259.
[9] J.F. Wang et al., J. Hepatol. 74 (2021) 627–637.
[10] Z.Y. Han et al., Adv. Funct. Mater. 33 (2023) 2302728.
[11] B. Wang et al., Nat. Commun. 13 (2022) 3821.

Please cite this article in press as: C. Zhang et al., Materials Today (2024), https://doi.org/10.1016/j.mattod.2024.04.001

[12] L. Galluzzi et al., Nat. Rev. Clin. Oncol. 17 (12) (2020) 725–741.
[13] S.Y. Guo et al., Sig. Transduct. Target. Ther. 8 (2023) 205.
[14] X. Guan et al., Nat. Commun. 13 (2022) 2834.
[15] Y.L. Chen et al., ACS Nano 17 (2023) 16620–16632.
[16] W.C. Wu et al., J. Am. Chem. Soc. 144 (2022) 19038–19050.
[17] X. Yang et al., Nano Today 38 (2021) 101109.
[18] T.W. Kao et al., J. Exp. Clin. Cancer Res. 42 (2023) 171.
[19] A.K. Moesta et al., Nat. Rev. Immunol. 20 (2020) 739–755.
[20] C.Q. Mao et al., Sci. Transl. Med. 14 (2022) eabh1261.
[21] X.Y. Li et al., Cancer Discovery 9 (2019) 1754–1773.
[22] Q. Chen et al., ACS Nano 17 (2023) 12087–12100.
[23] W.S. Liu et al., Adv. Sci. 10 (2023) 2206335.
[24] C.L. Xia et al., Mol. Cancer 22 (2023) 44.
[25] S.C. Ding et al., Mater. Today 37 (2020) 112–125.
[26] D.J. Irvine, E.L. Dane, Nat. Rev. Immunol. 20 (2020) 321–334.
[27] Z.R. Goddard et al., Chem. Soc. Rev. 49 (2020) 8774–8779.
[28] M.Z. Zou et al., Adv. Mater. 31 (2019) 1904495.
[29] L.Z. Feng et al., CCS Chem. 1 (2019) 239–250.
[30] T.X.Z. Liang et al., Angew. Chem. Int. Ed. 60 (2021) 11464–11473.
[31] Y. Chao et al., Nat. Biomed. Eng. 2 (2018) 611–621.
[32] Z.B. Yang et al., Adv. Mater. 34 (2022) 2108908.
[33] Q.W. Chen et al., Angew. Chem. Int. Ed. 59 (2020) 21562–21570.
[34] Z. Yang et al., Angew. Chem. Int. Ed. 61 (2022) e202209484.
[35] J.R. Seymour et al., Nat. Microbiol. 2 (2017) 17065.
[36] D.M. Karl et al., Nature 426 (2003) 32.
[37] A. Burlacot et al., Nature 605 (2022) 366–371.
[38] S. Ozugur et al., iScience 24 (2021) 103158.
[39] J.E. Cohen et al., Sci. Adv. 3 (2017) e1603078.
[40] Y. Evron et al., Horm. Metab. Res. 47 (2015) 24–30.
[41] V. Veloso-Gimenez et al., Front. Bioeng. Biotechnol. 9 (2021) 796157.
[42] H.H. Chen et al., Sci. Adv. 6 (2020) eaba4311.
[43] G.P. Chen et al., Sci. Adv. 9 (2023) eadg3478.
[44] A. Antonucci et al., Nat. Nanotechnol. 17 (2022) 1111–1119.
[45] X. Zhou et al., Sci. Adv. 6 (2020) eabc5237.
[46] R.L. Qi et al., Angew. Chem. Int. Ed. 60 (2021) 5759–5765.
[47] X.J. Li et al., ACS Sustainable Chem. Eng. 8 (2020) 7600–7608.
[48] D.N. Zhong et al., Theranostics 11 (2021) 3580–3594.
[49] X.H. Yan et al., Sci. Robot. 2 (2017) eaaq1155.
[50] F.Y. Zhang et al., Nat. Mater. 21 (2022) 1324–1332.
[51] C.J. Ren et al., ACS Nano 17 (2023) 14161–14175.
[52] M. Morita et al., Appl. Biochem. Biotechnol. 87 (2000) 203–218.

Please cite this article in press as: C. Zhang et al., Materials Today (2024), https://doi.org/10.1016/j.mattod.2024.04.001